Local lattice distortions in $La_{1-x}Sr_xMnO_3$ studied by pulsed neutron scattering

Despina Louca* and T. Egami
Department of Materials Science and Engineering and Laboratory for the Research on the Structure of Matter, University of Pennsylvania, Philadelphia, Pennsylvania 19104

(Received 10 November 1997; revised manuscript received 29 July 1998)

Pulsed neutron-diffraction measurements were carried out on powder samples of $La_{1-x}Sr_xMnO_3$ ($0 \leqslant x \leqslant 0.5$) in order to study the local atomic structure of this system known for its colossal magnetoresistance phenomenon. The results are analyzed in terms of the atomic pair-density function to elucidate the role of local lattice distortion in the magnetic and charge transport properties. It is shown that the Jahn-Teller (JT) distortions are locally present even when the crystallographic structure suggests otherwise, and indicate the formation of small lattice polarons in the insulating phase. Local JT distortions are observed even in the metallic phase up to $x = 0.35$, suggesting that the charge distribution in the metallic phase just above the metal-insulator transition may not be spatially uniform. It is possible that charges are partially confined by spin and lattice resulting in microscopic separation of the charge-rich and charge-poor regions. [S0163-1829(99)02209-2]

I. INTRODUCTION

In spite of extensive studies on the perovskite manganites $La_{1-x}A_xMnO_3$ (A = Ca, Sr, Ba, or Pb) which exhibit the colossal magnetoresistance (CMR) phenomenon,[1] a number of fundamental issues remain unresolved. These include the nature of the metal-insulator (MI) transition and the role of the Jahn-Teller (JT) distortion on charge localization. The possibility of lattice involvement through polaron formation was suggested by Millis *et al.*[2] by showing that the existing double-exchange (DE) model could not fully account for the observed properties. A number of studies suggested the involvement of the lattice in the form of structural distortion or anharmonicity,[3–10] but the structural evidence on the presence of polarons has been less than fully convincing, and their involvement in the properties needs further elucidation. In the present paper, we describe our results of pulsed neutron powder-diffraction measurements which delineate the role of the lattice in the magnetic and transport properties in this mixed-ion system, by explicitly showing the existence of lattice polarons directly related to the JT distortion. A part of this work was reported earlier.[11,12]

Manganites have attracted considerable attention recently because of their potential application in magnetic recording.[1] However, varieties of magnetic and transport properties have been known for some time.[13,14] In these compounds low-temperature ordering of Mn spins changes from antiferromagnetic (AFM) to ferromagnetic (FM) with the degree of hole doping x,[13] with a spin-glass or noncollinear ferromagnetic phase often appearing for intermediate compositions.[14] Electrical conductivity also changes with x and temperature T, from an insulator for low values of x to a metal with increased x.[13–15] Over a certain range of x the paramagnetic (PM) to FM transition is concomitant with the insulator-to-metal (I-M) transition.[13–15]

Zener[16] suggested a possible connection between ferromagnetism and electrical conduction in terms of the DE interaction mechanism, and this idea was expanded upon later.[17–19] The simple DE model assumes a homogeneous ferromagnetic state and a fully periodic charge distribution. However, as it was pointed out by Ref. 2, the DE model predicts an increase in the resistivity with decreasing temperature in the vicinity of T_c, while the reverse of that has been observed experimentally; namely, resistivity decreases with decreasing temperature below T_c. Furthermore the observed resistivity is much higher than expected for the DE mechanism. Millis *et al.*[2] proposed that the additional resistivity is produced by the strong electron-lattice coupling leading to polaron formation in the insulating paramagnetic phase.

We carried out a detailed investigation on a number of powder samples of $La_{1-x}Sr_xMnO_3$ with $0.0 \leqslant x \leqslant 0.5$ by pulsed neutron scattering, paying particular care to the oxygen stoichiometry. In this paper we describe our findings on the dependence of the local structure on temperature and composition. Through the pair-density function (PDF) analysis, we show a clear departure of the actual local structure from the average crystallographic structure. These differences are particularly notable in the MnO_6 octahedron, and can be interpreted in terms of the local JT distortion. It appears that these local lattice variations are induced by the presence of charges. In the paramagnetic phase our results are consistent with the self-trapping of a hole at the Mn ion without the JT distortion, forming a small polaron represented by a Mn^{4+} ion. At low temperatures the charges are less localized, but even in the metallic phase the local JT distortions are observed up to $x = 0.35$, suggesting possible spatial variation in charge distribution. The observed local structure is in disagreement with the simple DE model.

We also provide evidence of anomalous lattice dynamics in the region of the M-I transition. From the pulsed neutron experiment, one can obtain qualitative information on the range of dynamics by comparing information obtained from different angles of diffraction. In this way, we conjecture that near the M-I transition the decoupling of the charge dynamics from the local lattice dynamics must take place. Our results suggest that in the insulating phase the carriers are self-trapped forming polarons, while they no longer follows the dynamics of the local lattice distortion in the metallic phase.

The outline of this paper is as follows: In Sec. II, an

introduction to the experimental technique and data analysis is given. In Sec. III, we present our results on the local structure of $La_{1-x}Sr_xMnO_3$. We examine how the local atomic structure changes with hole doping and temperature. Section III includes a discussion on the dynamics in the system. Lastly, in Sec. IV, we discuss the implications of our results in terms of the interplay between charges and the lattice, and how this could lead to the explanations of the observed properties of the system.

II. EXPERIMENT

A. Data collection and analysis

The pulsed-neutron powder-diffraction data were collected in the time-of-flight (TOF) mode with the Glass Liquid and Amorphous Materials Diffractometer (GLAD) at the Intense Pulsed Neutron Source (IPNS) of the Argonne National Laboratory, at temperatures ranging from 10 to 350 K. Approximately 14 g of the sample in a finely powdered form was used in each experiment and loaded in a vanadium can with helium gas as a heat exchanger. All measurements were performed with the sample mounted on a displex refrigeration system in an evacuated chamber. The data were corrected for absorption, incoherent scattering, multiple scattering, and inelastic scattering (Placzek correction) to obtain the structure function, $S(Q)$, ($Q=4\pi \sin\theta/\lambda$, where Q is the momentum transfer, θ is the diffraction angle, and λ is the wavelength of a neutron) up to $Q_{\max}$ of 35 Å^{-1}. The high-Q portion of the data is particularly important in this study because it carries information regarding small local displacements of atoms.

The powder samples were prepared by the solid-state reaction method. Using stoichiometric amounts of pure $SrCO_3$, MnO_2, and La_2O_3, samples were pressed into pellets and initially fired under flowing oxygen between 1250 and 1300 °C for a period of five days in average. They were ground and fired repeatedly until a single phase was achieved. The samples were subsequently annealed in a controlled oxygen environment (with a $PO^2 \approx 10^{-5}$) at 1000 °C and quenched from this temperature to ensure the oxygen stoichiometry. Characterization of the purity and stoichiometry of the single phase was done using x-ray-diffraction and energy-dispersive x-ray analysis analysis. With the help of thermogravimetric analysis (TGA) the oxygen stoichiometry was determined to be 3.00 ± 0.01. The magnetic transitions of the samples were confirmed by the susceptibility measurements to be in agreement with the published data.

The PDF, $\rho_0 g(\mathbf{r})$, is calculated by Fourier transforming the structure function, $S(Q)$, in the following way:

$$\rho_0 g(r) = \rho_0 + \frac{1}{2\pi^2 r}\int_0^\infty Q[S(Q)-1]\sin(Qr)dQ \qquad (1)$$

where ρ_0 is the average atomic number density of the sample. Theoretically the Fourier integration should be carried out to $Q=\infty$, but in reality it has to be terminated at a finite value of Q determined by the wavelength of the probe, λ ($Q<4\pi/\lambda$). Premature termination of the integral (1) results in spurious oscillations called termination errors. However, because of the Debye-Waller factor, $S(Q)$ converges to unity at large-Q values. As long as the $S(Q)$ is determined up to a high enough value of Q to ensure this convergence, the termination errors can be minimized. Usually a cutoff of 30–40 Å^{-1} is sufficient to avoid termination errors that originate from the Fourier transformation.[20,21] While such a high value of Q is difficult to attain with conventional x-ray sources or thermal neutron sources, they can readily be obtained with the pulsed neutron source or the synchrotron-radiation source.

The PDF is a real-space representation of atomic pair-density correlations. The PDF analysis has been used for the studies of glasses, liquids[22,23] as well as other crystalline materials,[24–26] and it has been proven effective and reliable in determining the local atomic structure. Unlike standard crystallographic techniques such as the Rietveld method that focus on the Bragg peaks and carry out a structure refinement in the Q range typically up to 12 Å^{-1}, the PDF analysis takes into account the full structural information including the diffuse scattering intensities as well as the Bragg peaks up to high values of Q. Thus the PDF can accurately describe the local structure in periodic as well as aperiodic systems, and this technique can provide information regarding any local deviations from their average crystallographic structure. While it is possible to include some structural disorder in the crystallographic analysis, for instance by introducing partially occupied sites, the spatial correlation among the partially occupied sites cannot be determined by crystallographic methods that presume periodicity. The PDF method is therefore ideal for describing any anharmonic or locally correlated atomic displacements in the lattice. Details of this procedure are described in Refs. 20 and 21. In the present work we encountered a special challenge because of the negative neutron-scattering length b of Mn. When elements with positive and negative neutron-scattering lengths are mixed the coherent scattering intensity is weak, and the background correction becomes very important. While the sample-dependent background due to the double scattering from the sample and the environment is normally neglected, we found it becomes significant in this case due to the lower signal-to-background ratio. The intensity of such background was carefully determined by studying standard samples with different average scattering lengths.

B. Calibration with standard samples

The accuracy of the instrument was tested using nickel and $SrTiO_3$ powders as standards. Ni serves as a good standard because it is a strong neutron scatterer and its structure (fcc) is well known. In Fig. 1, the PDF determined from the diffraction data for the Ni powder (symbols) at $T=10$ K is compared to a model PDF (solid line) determined from the fcc structure of Ni. The model PDF consists of δ functions at positions corresponding to interatomic distances, convoluted with a gaussian function that represents thermal and zero-point quantum fluctuations. The width of the gaussian function ($\sigma=0.064$ Å) that maximizes the agreement between the experimental PDF and the model PDF is fully consistent with the known amplitude of the zero-point oscillation for Ni.[27] As can be seen, the PDF determined from the diffraction data agrees quite well with the model PDF.

Since Ni is ferromagnetic the PDF in Fig. 1 contains magnetic contributions, but they are practically invisible. This is

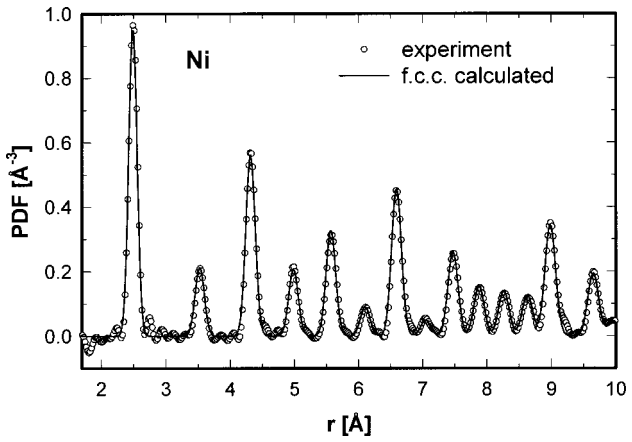

FIG. 1. The PDF of nickel determined at 10 K (symbols) compared to a model PDF (solid line) for the fcc structure. The model and measured PDF's are in very good agreement.

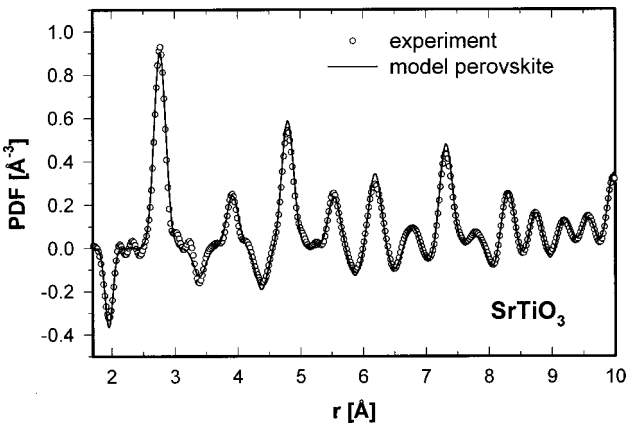

FIG. 2. The PDF of $SrTiO_3$ determined at 10 K (symbols) compared to a model PDF (solid line) for the Pm3m perovskite structure. For the model PDF the lattice constant of 3.91 Å and the peak width of $\sigma = 0.062$ Å were used. The model PDF agrees very well with the measured PDF.

partly because the magnetic moment of Ni is small ($0.6\mu_B$), while the value of b for Ni is large, making the magnetic contribution minuscule. But the more important and general reason that is relevant also for the study of manganites is that the magnetic moment is spread in space, reflecting the spatial extension of the $3d$ electrons. Consequently the magnetic form factor depends strongly on Q, and the PDF peak describing the magnetic correlation is much broader and weaker than the nuclear PDF peaks. The magnetic PDF can be determined by using spin-polarized neutrons and dividing $S(Q)$ through the magnetic form factor.[28]

$SrTiO_3$ can equally be used in this case as a standard, since it has the perovskite structure which can be directly compared to that of manganites. In addition this compound consists of a mixture of positive and negative scattering lengths just as the manganites. The PDF of a multielement system obtained by Eq. (1) is given by

$$\rho_0 g(r) = \rho_0 \sum_{\alpha,\beta} c_\alpha c_\beta \frac{b_\alpha b_\beta}{\langle b \rangle^2} g_{\alpha\beta}(r), \tag{2}$$

where c_α and b_α are the concentration and scattering length of the element α, $\langle b \rangle$ is the compositionally averaged scattering length, and $g_{\alpha\beta}(r)$ is the compositionally resolved partial PDF between elements α and β. Thus the negative b of Ti makes the PDF peaks involving Ti negative and easier to distinguish. In Fig. 2, the PDF of $SrTiO_3$ determined from the experimental data collected at 10 K is compared to a model PDF for the perovskite structure with $Pm3m$ symmetry. As can be seen, the model PDF is in very good agreement with the experimentally determined PDF. Along with the result for Ni, this result demonstrates the high accuracy of the pulsed neutron PDF with regard to the actual crystal structure determination. In fact the recent pulsed neutron study of $PbZrO_3$ demonstrated that the structure determination by the real-space modeling of the PDF is at least as accurate as the Rietveld refinement method for the atomic position parameters within the unit cell.[29]

The area under each peak corresponds to the coordination number represented by the peak at specific interatomic distances weighted by the scattering lengths of elements. The number of β atoms around an α atom is given by

$$N_{\alpha\beta} = 4\pi\rho_0 c_\beta \int_{\text{peak}} g_{\alpha\beta}(r) r^2 dr. \tag{3}$$

Thus if a peak is composed of distances between α and β alone, $N_{\alpha\beta}$ can be determined by integrating $4\pi r^2 \rho_0 g(r)$, which is usually called the radial distribution function (RDF), over the region incorporating the peak in question, and multiplying it by $\langle b \rangle^2 / c_\alpha b_\alpha b_\beta$. Table I lists the atomic distance and the coordination number for different neighbors in Ni and $SrTiO_3$. As seen in the Table both the atomic distances and coordination numbers are determined with high accuracy by this method of analysis. For $SrTiO_3$ only

TABLE I. Atomic distance and number of neighbors in Ni and $SrTiO_3$ determined from the PDF analysis compared to the expected values.

		Peak position (Å)		Number of neighbors	
Compound	Coordination shell	Expected	Measured	Expected	Measured
Ni	First	2.49	2.49	12	11.995
	Second	3.53	3.53	6	6.022
	Third	4.32	4.32	24	23.875
	Fourth	4.98	4.98	12	11.974
	Fifth	5.57	5.57	24	23.818
$SrTiO_3$	First (Ti-O)	1.95	1.95	6	5.97
	Second (O-O, Sr-O)	2.77	2.77	36	36.87

the first two PDF peaks are clearly separated from others and allow accurate determination of $N_{\alpha\beta}$. Other peaks partially overlap and cancel each other, making the determination less reliable. The error analysis for the coordination number is made by estimating the uncertainty in the PDF due to random and systematic errors in the data. These errors give rise to oscillations at very low values of **r**. By determining the root-mean-square (rms) of these oscillations one can estimate the RDF error and subsequently the error in the coordination number.

C. Dynamical considerations

The GLAD spectrometer consists of 231 position sensitive linear detectors grouped into 10 banks with the highest angle of diffraction at 125° and the lowest at 8°. Details of the instrument setup and data acquisition are described in Ref. 30. In the TOF diffraction experiment the neutron detectors do not have energy resolution. As a result both elastically as well as inelastically scattered neutrons are recorded at the detectors, and for each neutron the Q value is calculated from the time of flight and the detector angle assuming elastic scattering. In the event of inelastic scattering, the true momentum transfer Q is different from the assigned value Q'. Placzek[31] proposed a correction scheme to compensate for the distortions introduced in the data due to the inelastic scattering of neutrons using a ballistic approximation. While this scheme is reasonably successful when the inelastic scattering is caused by phonons, severe deviations can be observed when strong local modes of lattice vibration are present.[32] These deviations are quite notable for compositions near the I-M transition as we will describe below.

III. RESULTS

A. Undoped compound $LaMnO_3$

The PDF's of $LaMnO_3$ at two temperatures ($T=300$ and 10 K) were shown in Fig. 1 of Ref. 12. The Néel temperature of this compound is $T_N \approx 140$ K. The crystallographic structure is of monoclinic symmetry, $P2_{\|c}$.[33] In the presence of excess oxygen the symmetry becomes orthorhombic or rhombohedral (as will be discussed elsewhere[34]). This result agrees with Refs. 33–36, but disagrees with Ref. 37. The cause of such disagreement must be the extreme sensitivity of the structure on oxygen stoichiometry and the difficulty of determining the oxygen content accurately.

Crystal-field effects on a $Mn^{3+}(d^4)$ ion split the $3d$ level to the t_{2g} (triplet) and e_g (doublet) levels. Because of a strong Hund's coupling the spins of the d electrons are aligned, so that the t_{2g} level is filled for one spin by three electrons and the e_g level is singly occupied for the same spin orientation. Consequently the MnO_6 octahedron is Jahn-Teller (JT) distorted and is elongated in one direction ζ to produce a splitting in the e_g level. Because of this distortion the bond distances between manganese and oxygen atoms within each octahedron become unequal and split into short and long bonds. The bondlengths ranging from 1.87–2.00 Å constitute the short bonds and the bondlength of 2.11–2.22 Å corresponds to the long bonds as determined from the crystallographic analysis.[33] This split in the Mn-O distances is seen from the PDF's in Fig. 1 of Ref. 12 as the first negative peak centered about 1.93 Å (short bonds) with a shoulder to the right, at 2.16 Å (long bonds). Note that this peak is negative because the neutron-scattering length of Mn is negative while that of oxygen is positive and the PDF as seen from Eq. (2) is normalized by the scattering length of the elements. We should also note that the subpeak at 2.16 Å is partially concealed by the tail of the intense positive peak of La-O and O-O pairs at 2.55 Å and above, and consequently the number of Mn-O pairs represented under this subpeak cannot be determined accurately. On the contrary, the first peak at 1.93 Å overlaps slightly only with the subpeak for the long Mn-O bond, so that the area under this peak can be determined relatively accurately. The ambiguity in the area under the first peak due to the overlap with the small peak at 2.16 Å is actually quite small, well within the error of calculation.

In an ideal cubic perovskite structure, the second peak describes the La-O and O-O distances which is $1/\sqrt{2}$ times the lattice constant. In $LaMnO_3$, the La-O peak splits into three subpeaks at 2.55, 2.75, and 2.96 Å due to the octahedral tilting driven by the mismatch between the Mn-O and La-O bonds. Also the O-O peak is split into two peaks, at 2.75 Å representing four O-O bonds and at 3.0 Å for eight O-O elongated bonds, because of the JT distortion of the MnO_6 octahedron.

Up to room temperature the local atomic structure is virtually independent of temperature as shown in Fig. 1 of Ref. 12. This is partly because of its high Debye temperature,[38] but the Q termination and the decreased Q resolution at the high-Q range may have contributed to it. The increase in thermal vibrations with temperature gives rise to broader peaks but the area under the peak remains constant.

$LaMnO_3$ is antiferromagnetic at low temperatures, and the neutron-diffraction pattern at 10 K shows extra magnetic peaks which are absent at 300 K. In spite of the appearance of these magnetic peaks at low temperatures no signature of magnetic correlation is observable in the PDF, for the reasons discussed earlier. It should be noted that the magnetic PDF affects only the Mn-Mn peaks, and do not affect the first Mn-O peak in the PDF at all, since the magnetic polarization of the oxygen atom is zero as required by symmetry. Even for the Mn-Mn peak the change in the PDF is rather small as evidenced by a very small change of the peak at 3.93 Å. The amplitude in PDF due to the magnetic correlation at this peak is estimated to be ~ 0.02 Å^{-3} which is almost at the level of the noise. In the PM phase the paramagnetic scattering produces, upon Fourier transformation, merely the autocorrelation of the spin density of each atom. This effect dies off quickly with r in the PDF, and at interatomic distances and beyond it is negligibly small.

B. The local Jahn-Teller effect

From the crystallographic analysis, it has been reported that the structure undergoes a transition from monoclinic (M) ($P2_{\|c}$) to orthorhombic (O) ($Pbnm$), at $x=0.1$, and then to a rhombohedral (R) ($R\bar{3}C$) symmetry at $x=0.175$ accompanied by an apparent loss of the macroscopic signature of the JT distortions in the R phase.[33] Shown in Fig. 1 of Ref. 12 is the PDF calculated for the model structure of $LaMnO_3$ with the monoclinic crystallographic symmetry. The model was

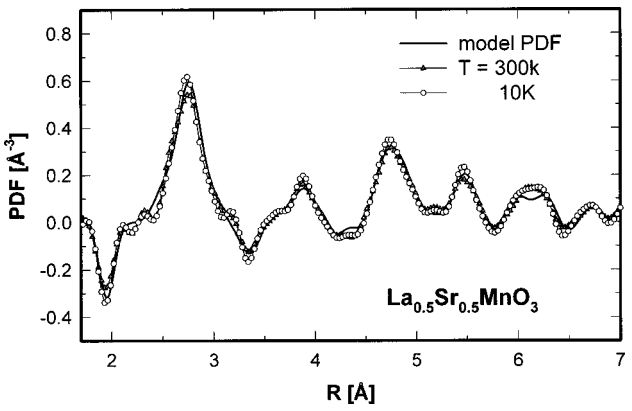

FIG. 3. The PDF of $La_{0.5}Sr_{0.5}MnO_3$ determined at 300 and 10 K. The local structure shows very little temperature dependence. The PDF's are in very good agreement with the model PDF for the nearly cubic structure for this composition.

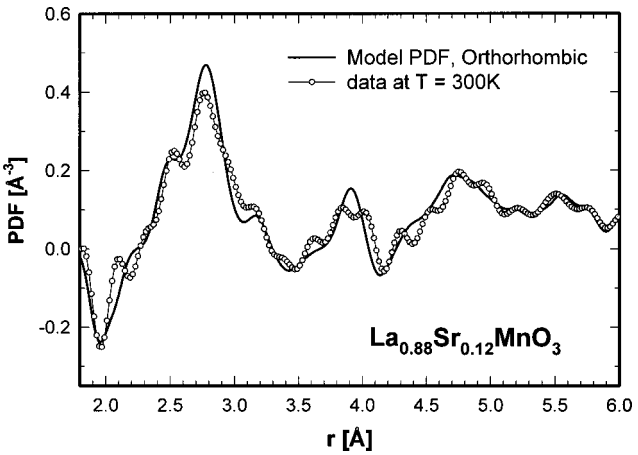

FIG. 4. The PDF for the orthorhombic model with Pnma symmetry compared to the experimentally determined PDF of the 12% sample of the same symmetry. Below 5 Å the model PDF disagrees significantly with the data. Note that the JT distortion is very small for the model PDF.

created with the atomic coordinates and unit-cell dimensions determined by the Rietveld refinement.[33] The model PDF is the sum of the partial PDF's of all pairs of atoms in the structure as in Eq. (2). The full width at half maximum value of the Gaussian function to simulate thermal and quantum zero-point lattice vibrations was 0.14 Å which is similar to the one used in the model PDF fitting to the experimentally determined PDF of MnO. This value is consistent with the amplitude of oscillations that can be determined from the Debye temperature $[\Theta_D = \sim 400\,\mathrm{K}$ in the case of $La_{0.8}Ca_{0.2}MnO_3$ (Ref. 38)]. The estimated error in the PDF from the statistical error[26] is 0.012 Å^{-3} in the range shown. The experimental PDF's at both temperatures shown in Fig. 3 are in excellent agreement with the model.

At very high doping levels, a weak temperature dependence is observed and the JT peak at 2.16 Å is reduced considerably if present at all. In Fig. 3, the PDF's of $La_{0.5}Sr_{0.5}MnO_3$ sample determined at 10 and 300 K are shown. The local structure changes with temperature very little as seen by the small changes in the peak intensity. Note that the JT peak around 2.2 Å appears to be completely gone at this composition as its intensity is not higher than the oscillation ripples due to noise.

At intermediate doping levels, one can observe the transition from the cooperative, ordered JT state, to the disordered JT state with random orientation of the local JT distortion with no macroscopic JT distortion, and finally to the complete absence of the local JT distortion. In Fig. 4, the measured PDF of the 12% sample is compared to a model PDF for the orthorhombic symmetry, and in Fig. 3 of Ref. 12 the PDF of the 20% sample is compared to the PDF of a rhombohedral model. The model parameters were obtained from Ref. 33. In both cases the measured PDF's compare reasonably well with the model PDF's beyond 4 or 5 Å, indicating that the average and local structures agree in the long-range order. However, strong differences are quite notable, particularly below 3 Å. In terms of the agreement factor A defined by

$$A = \left[\frac{\int_{r_1}^{r_2} [g_{\mathrm{exp}}(r) - g_{\mathrm{mod}}(r)]^2 dr}{\int_{r_1}^{r_2} dr} \right]^{1/2}, \qquad (4)$$

where $g_{\mathrm{exp}}(r)$ and $g_{\mathrm{mod}}(r)$ are the experimental and model PDF's, the value of the A factor is about two times larger in the short range of 1.5–5.5 Å ($A = 0.257$) than for the longer range of 5.5–9.4 Å ($A = 0.139$). Clearly the crystallographic models cannot adequately describe the local Mn-O and La/Sr-O bond lengths. In the model structures the distributions of the Mn-O and La/Sr-O bond lengths are narrower, making the model PDF peaks sharper and taller than in the measured PDF. For instance in the model structure of the 12% sample the JT distortion is much reduced compared to the undoped sample (to about 1/4), so that all the Mn-O lengths are similar. In contrast, in the experimentally determined PDF, the subpeak for the long Mn-O bond, the JT peak, is still clearly distinguishable, indicating that locally the magnitude of the JT distortion has not been reduced. In the crystallographic rhombohedral structure the JT distortion is completely absent, while the PDF of the 20% sample still shows a negative peak at 2.25 Å, indicating that the JT distortion is locally present. In summary, while the JT distortion quickly decreases with Sr doping in the crystallographic structure, in the real structure the JT distortion locally persists well past the phase boundary into the rhombohedral phase. However, at the Sr content as high as 50% the local JT distortion is absent as can be seen from the agreement of the model PDF with the experimental PDF as shown in Fig. 3.

The local structure described by the PDF is inconsistent with the crystallographic structure over a wide range of composition including the metallic compositions up to 30% which are of rhombohedral symmetry. The composition dependence of the positions of the two Mn-O peaks is plotted in Fig. 4 of Ref. 12, and is compared with the Mn-O distances deduced from the lattice constants of the crystal structure.[15] While the crystallographic structure suggests that the JT distortion of the average lattice is quickly suppressed by Sr and disappears around $x = 0.17$, it is clear that locally the magnitude of the JT distortion is unchanged, and the local JT distortion is present even in the rhombohedral phase. Since the PDF is a spherically averaged quantity due to powder averaging, it records the local JT distortion in any

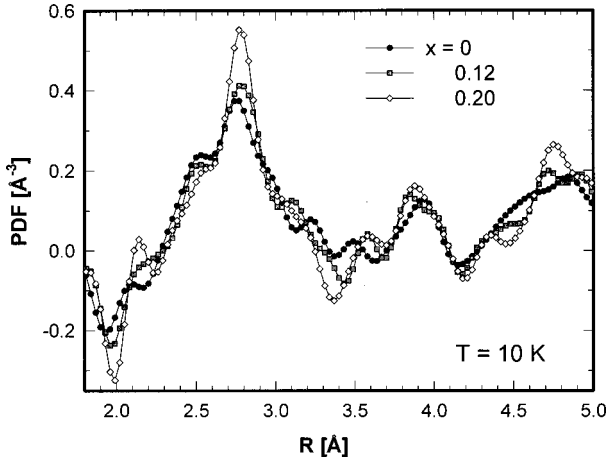

FIG. 5. The PDF's of $La_{1-x}Sr_xMnO_3$ for $x=0.0$, 0.12, and 0.20 at 10 K indicate stronger composition dependence than at room temperature.

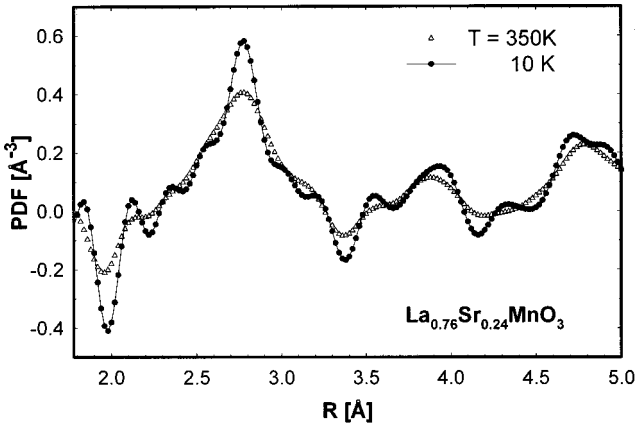

FIG. 6. The PDF for the rhombohedral model with $R\bar{3}C$ compared to the measured PDF of $La_{0.76}Sr_{0.24}MnO_3$, determined at 350 and 10 K. The intensity under the peaks increases considerably with decreasing temperature. Note that in the model PDF, a very sharp Mn-O peak is observed at 1.95 Å whereas in the data PDF the Mn-O peak has a subpeak due to the long Mn-O bonds.

orientation. The changes in the long-range order could be brought about by randomization of the orientation of the local JT distortion. This result is consistent with the extended-x-ray-absorption-fine-structure measurement except for the actual Mn-O bond lengths,[9] and with the results of high-resolution microscopy that suggests that two types of bonds are present in the metallic samples.[39] We note that these local effects cannot be explained in terms of the difference in the Sr and La ionic sizes [1.36 Å for La^{3+} and 1.44 Å for Sr^{2+} (Ref. 40)]. The changes in the perovskite tolerance factor[41] $t=d_{\text{La/Sr-O}}/\sqrt{2(d_{\text{Mn-O}})}$ with composition is too small to account for the structural transition from the monoclinic to rhombohedral structure. On the other hand, the JT distortion is caused by the singly occupied e_g level. Since at the phase boundary ($x=0.17$) the e_g level is still 83% singly filled, it is not totally surprising if local JT distortions are seen at some of the Mn ions.

C. The anti-JT distortion

While the changes in the PDF peak positions with composition are rather minor, the peak intensity depends on composition more strongly at low temperatures as indicated by the PDF's at $T=10$ K shown in Fig. 5. For instance, the height of the peak at 1.95 Å and that at 2.75 Å are considerably enhanced with the increase in Sr doping. The change in the intensity of the PDF peaks with temperature increases with doping as shown in Fig. 6, as is illustrated by the temperature dependence of the PDF of $La_{0.76}Sr_{0.24}MnO_3$ for $T=350$ and 10 K. In comparison to the pure compound (Fig. 1 of Ref. 12), more structural changes with temperature are apparent evidenced by the change in the height of the peaks. In many of the peaks, a significant increase in height with cooling is seen. For instance, the height of the 2.75 Å peak increases by as much as 30% between 300 and 10 K, similar to what has been observed for $La_{1-x}Ca_xMnO_3$.[3] Such a large change cannot be accounted for by the Debye-Waller factor. Note also that the JT peak (the long Mn-O bonds) at 2.25 Å is fairly well defined at 10 K for this composition.

The change in the intensity of the first negative peak is more readily expressed in terms of the composition dependence of the number of nearest O neighbors for Mn. In the undoped compound $LaMnO_3$, because of the JT distortion of the Mn^{3+} ion the number of short bonds under the first negative peak is four (4). For comparison, without the JT distortion as is the case in $SrMnO_3$ (Mn^{4+}), $N_{\text{Mn-O}}$ would be six (6). The number of close O neighbors for Mn, $N_{\text{Mn-O}}$, can be determined by carrying out the integration in Eq. (3) from r_1 to r_2 covering the first negative peak of the PDF. Since the end portion of this peak overlaps with the peak of the long Mn-O bonds, it is necessary to choose carefully the upper cutoff limit of integration r_2, while the value of r_1 is more clearly defined by the start of the first peak at 1.76 Å. Figure 7 shows the relation between the $N_{\text{Mn-O}}$ determined from the first PDF peak at 300 K to the r_2 cutoff value. The valley between the first and second subpeaks of the first peak is located at 2.10 Å. Indeed the upper cutoff value of 2.10 Å for $T>T_N$ gives the value of $N_{\text{Mn-O}}$ at $T=300$ K for $LaMnO_3$

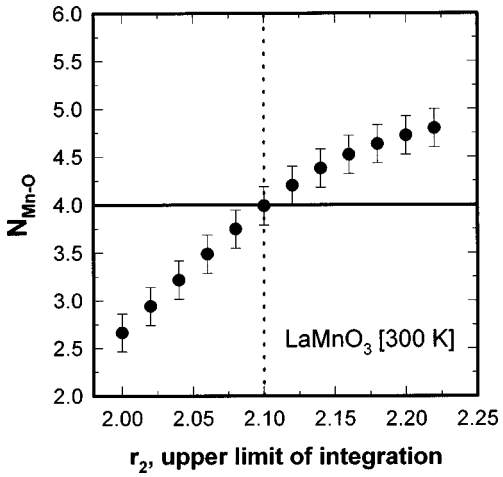

FIG. 7. $N_{\text{Mn-O}}$ as a function of the upper limit of integration $\mathbf{r}_2$ for $LaMnO_3$ at 300 K. The cutoff value r_2 of 2.15 Å corresponds to the valley between the two Mn-O subpeaks, and correctly gives $N_{\text{Mn-O}}$ very close to 4. Thus r_2 was chosen to be 2.15 Å for all data at room temperature or above T_c. In the case of the 10 K data a cutoff value of 2.10 Å was chosen by the similar process.

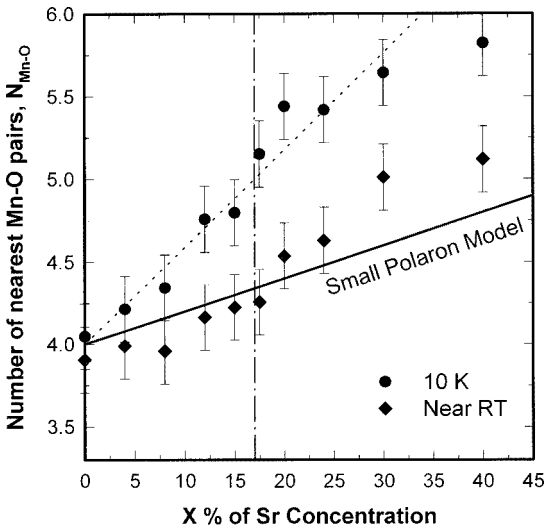

FIG. 8. The number of nearest Mn-O neighbors, $N_{\text{Mn-O}}$, as a function of Sr doping at 300 and 10 K. The solid line represents a small-polaron model in which the charges are localized at Mn^{4+} sites. At $T > T_c$, T_N, the data points are close to the small-polaron line but below, the data points deviate upwards from the small-polaron line. The simple double-exchange (DE) model predicts $N_{\text{Mn-O}} = 6$ beyond 17% (M-I transition), while the 10 K data suggest $N_{\text{Mn-O}} = 5$ at the M-I transition, and can be fit by the dotted line which reaches $N_{\text{Mn-O}} = 6$ only at $x = 0.35$. This result suggests that in average the charge is shared by about three Mn sites.

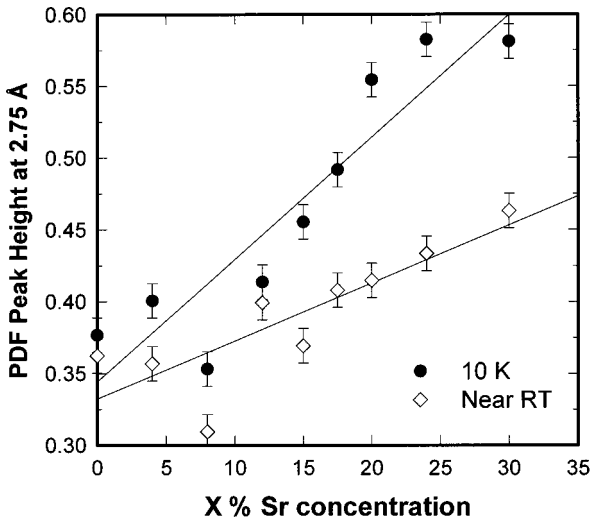

FIG. 9. Composition dependence of the height of the PDF peak at 2.75 Å. This peak is due partially to the short O-O distances, and its increase mainly represents the increase in the Mn sites with no JT distortion. Thus this result reinforces the result given in Fig. 8. In particular, the ratio of the slope for the 300 K data and that for the 10 K data corresponds to the ratio of the polaron size.

very close to 4 as it should be, underscoring the accuracy of the present analysis. At $T = 10$ K, we chose the cutoff of 2.08 Å, a slightly lower value reflecting the reduced PDF peak width. The error in the $N_{\text{Mn-O}}$ value is calculated from the error propagated from $\rho_0 g(r)$ described above in the standard calibration.

The composition dependence of $N_{\text{Mn-O}}$ is shown in Fig. 8, for the data collected at 300 K or above T_c, T_N and at 10 K. The solid line labeled ''the small-polaron model'' connects $N_{\text{Mn-O}} = 4$ for $x = 0$ representing Mn^{3+} in $LaMnO_3$, and $N_{\text{Mn-O}} = 6$ at $x = 1.0$ representing Mn^{4+} in $SrMnO_3$. This linear relation between $N_{\text{Mn-O}}$ and the hole concentration assumes that the doped hole is completely localized within one octahedron forming a single-site small polaron, i.e., the local Mn^{4+} site, so that the system is made of a mixture of Mn^{3+} and Mn^{4+} ions. The room-temperature data up to 24% (PM state) are close to the single-site polaron line. The points at 30 and 40% are slightly above the small-polaron line, but this is probably because the data were collected slightly below T_c. The presence of single-site polarons in the PM state is in agreement with the theoretical prediction in terms of the entropical effect.[42] The low-temperature data, however, significantly deviate upward from the small-polaron model. The values of $N_{\text{Mn-O}}$ at $T = 10$ K increases more rapidly with x as shown in Fig. 8, and extrapolates to $N_{\text{Mn-O}} = 6$ around $x = 0.35$. The implication of this result will be discussed later.

A similar phenomenon is observed with the composition dependence in the peak height of the O-O peak at 2.75 Å (Fig. 9). As we discussed above in the JT distorted MnO_6 octahedron 2/3 of the O-O distances are elongated to 3.1 Å, and do not contribute to the 2.75 Å peak. The increase in the height of this peak with doping reflects an increase in the density of the short O-O bonds, thus of the MnO_6 octahedra without the JT distortion. The rate of increase in the peak height at 10 K is faster than at 300 K. However, we need to note here that other factors contribute to this peak including the difference in the La-O and Sr-O bond lengths along with changes in the octahedral tilting. This does not apply to the case of the first Mn-O peak because this peak is entirely comprised of the short Mn-O pairs and is not affected by the tilting of the octahedron.

The incremental change in the number of nearest oxygen neighbors to manganese with temperature is shown in Fig. 10 for the case of the $La_{0.8}Sr_{0.2}MnO_{3.02}$ sample. At this composition, both an I-M transition as well as a PM to an FM

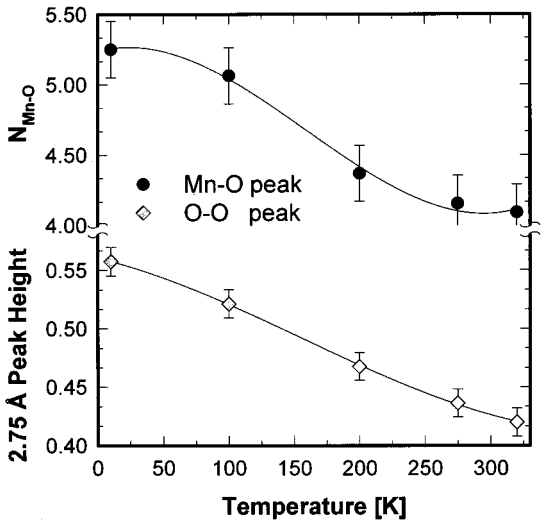

FIG. 10. Top: $N_{\text{Mn-O}}$ as a function of temperature for the 20% sample. It is constant at high temperatures but quickly rises with decreasing temperature. Bottom: The height of the PDF peak at 2.75 Å which includes the O-O pair. Its relation to temperature is similar to that of the $N_{\text{Mn-O}}$ value.

transition occur with lowering the temperature. $N_{\text{Mn-O}}$ is only weakly temperature dependent at very high temperatures, quickly rises below T_c, and eventually levels off at low temperatures. A very similar dependence to temperature is exhibited by the PDF peak height of the O-O peak also shown in the figure. Similar changes in the peak height were observed for the La-Ca system.[3]

D. Dynamics in the critical region

The PDF's of the compound with 15% Sr determined at 300 and at 10 K were found to exhibit rather irregular changes with temperature not seen in other compositions. Commonly, the temperature-dependent effects would involve a change in the height of the PDF peaks but shifts in the peak position were seen for this composition. This irregular behavior is due to a particular dynamic effect of the spectrometer and not due to a real structural change. As we mentioned above, the TOF spectrometer without a chopper such as the GLAD cannot differentiate inelastically scattered neutrons from the elastically scattered neutrons. As a consequence the determined structure function $S(Q)$ represents an integral,

$$S(Q)=S[Q(\omega=0)]=\int_{-\infty}^{\infty} S(Q(\omega),\omega)d\omega, \qquad (5)$$

where $S(Q,\omega)$ is the dynamic structure factor. If Q is independent of ω the Fourier transform of $S(Q)$ corresponds to the instantaneous (same-time) PDF, or a snapshot. In the TOF spectrometers, however, Q is weakly dependent on ω, and this produces complications.

If the lattice excitations are all delocalized phonons, the correction can be made reasonably well by the procedure proposed by Placzek,[31] but when there are strong localized dynamic lattice modes the Placzek correction is not sufficient, and the Fourier transform will become distorted.[32,43] This spurious distortion depends upon the detector angle, so that if the PDF varies with the detector angle we know that the system has local dynamic distortion. Note that if the structure is static a change of the detector angle affects only the relation between the time of flight and Q, leaving $S(Q)$ unaffected, so that the PDF is independent of the detector angle. As shown in Fig. 11 the PDF's of $x=0.15$ at 300 K show significant variations as a function of the detector angle. In this figure each PDF was calculated using the data from the detectors located up to the 2θ value shown. On the contrary, as shown in Fig. 12 the PDF's for the 0% sample show very little dependence on the detector angle.

Such a strong dependence of the PDF on the detector angle was observed only for the $x=0.15$ sample. The PDF for the sample with $x=0.175$ showed much weaker dependence, while the PDF's for other samples showed practically no dependence on the detector angle. Note that these compositions are in the close vicinity of the I-M transition. Thus the dynamical phenomena are restricted only to the region of the I-M transition. The energy scale associated with the local dynamics that would cause distortions in the PDF is about 20 meV for GLAD as discussed in detail elsewhere.[32] Thus the polarons are either static or moving at an energy scale much smaller than 20 meV, in the composition ranges away from the I-M transition.

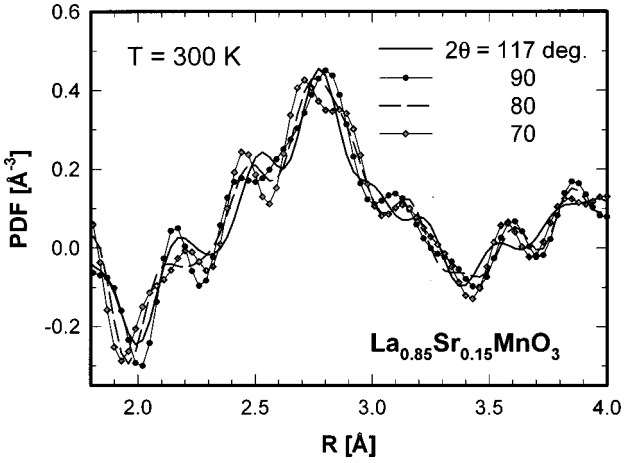

FIG. 11. The PDF of the 15% sample determined at different angles of diffraction. Data are integrated up to the 2θ values shown. Many changes are seen as the maximum diffraction angle is varied, suggesting that Q-dependent dynamic events occur in the structure. The range of this local lattice (nonphonon) dynamic is of the order of 20 meV.

IV. DISCUSSION

A. The evidence of polarons

The results of the PDF analysis of $La_{1-x}Sr_xMnO_3$ described above show convincingly that the local structure of the Sr-doped samples is deviated from the crystallographic structure. This also implies that the structure is spatially inhomogeneous in the time scale of the neutron TOF spectrometer. In particular, the JT distortions of the MnO_6 octahedra locally remain strong in spite of Sr doping. Much of the changes in the crystallographic structure due to Sr doping, including the phase change from the orthorhombic to rhombohedral structure, are brought about by the increased ran-

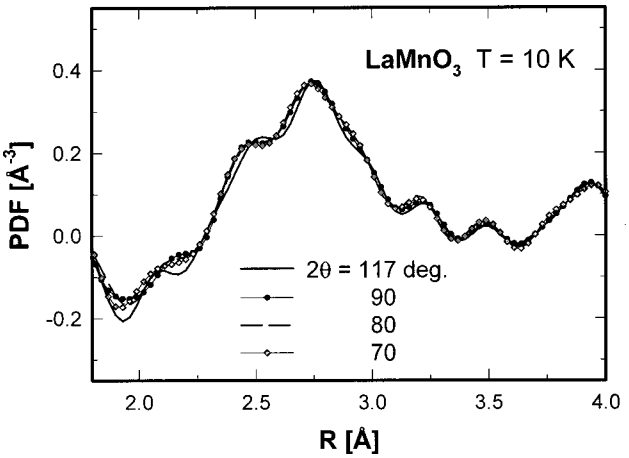

FIG. 12. The PDF of the undoped sample determined at different angles of diffraction. All PDF's are almost identical with the exception of the highest angle due to the difference in the value of $Q_{\max}$. This indicates that no local lattice dynamics with the energy above a few meV are present in this composition.

domization of the local orientation of the JT distortion with increasing Sr concentration, and not by the total disappearance of the JT distortion at the orthorhombic to rhombohedral transition.

However, doping causes some Mn ions locally to have no or reduced JT distortion. Above T_N or T_c the density of the Mn sites without the JT distortion is roughly equal to the charge (hole) density introduced by Sr doping. Thus it is only natural to conclude that the absence of the JT distortion, or the anti-JT distortion, is a direct consequence of the presence of charges. Indeed if a hole is localized on a Mn atom, changing it from Mn^{3+} to Mn^{4+}, the local JT distortion will disappear. Therefore, we conclude that the Mn sites without the local JT distortion represent the Mn^{4+} ions, or the single site lattice (and possibly spin) polarons.

Well below the magnetic transition temperature, on the other hand, more Mn sites have no local JT distortion than above T_N or T_c. In the simple DE model the ferromagnetic state is assumed to have a uniform structure that enables rapid charge hopping from one site to another.[17] All octahedral sites are assumed to be equivalent, with $3+x$ charges per Mn site, and all the Mn-O bonds are of the same length in the metallic regime since charges are shared equally by all Mn sites. Therefore $N_{\text{Mn-O}}$ should be equal to 6 in the metallic phase beyond the I-M transition (17% Sr) within the DE model.

A comparison of the data at 10 K to the predictions by the DE and the small-polaron models clearly indicates that a state not described by either model must exist at low temperatures. The charge carrier is neither totally delocalized in the metallic state as implied by the DE model nor fully localized to one site as in the small-polaron model. A fit to the data points at $T=10$ K shows that the coordination of 6 is reached at $\sim$35% of Sr doping with a slope that is about three times that of the single-site polaron line. This means that the density of the Mn sites without the JT distortion is three times the charge density. Thus the charge must be shared in average by about three Mn sites. In other words at $T \ll T_c$, T_N, polarons are more extended than at high temperatures with the size covering three Mn sites. Additional evidence on the size of the polaron is provided by the change in the density of O-O pairs under the PDF peak at 2.75 Å shown in Fig. 9. This PDF peak height changes more rapidly with x well below T_c or T_N than above, as is fully consistent with the observed changes in the density of short Mn-O pairs as a function of x. Thus both of these data imply that the size of the polaron below T_c, T_N is larger than above. Therefore, the simple DE model does not fully describe the nature of the metallic state in the CMR manganites.

The mechanism to create the three site polaron may be understood in the following way. $LaMnO_3$ has a layered antiferromagnetic structure with the alternating spin polarization along the c axis. When a hole is introduced in the system by doping, it will try to align the spins locally. This can be most simply achieved by flipping the spin at one Mn site which makes it parallel to the spins in the layers above and below. Once this happens the charge can easily move along the c axis among the three sites with parallel local spins. Also the ferromagnetic order in the layer may induce the orbital alignment of three sites in the layer, again allowing the hole to move freely within. Incidentally it is also interesting to note that other systems such as EuO become ferromagnetic in the complete absence of the DE interaction.[44]

Note that the lattice distortion described here is different from the one proposed by Billinge *et al.* who assumed polarons are represented by isotropic (breathing mode) lattice contraction.[3] In the present work the polarons clearly are characterized by the absence of local JT distortion. They based their claim on the study of the change in the PDF across the M-I transition temperature. However, within the temperature range chosen (36 K) the change in the PDF was very small, almost at the level of the noise. Thus it is difficult to reach a reliable conclusion based upon such a small change. In the present study the conclusion was obtained by an extensive study of the local structure over a wide range of composition. It is also possible that the relatively low-Q termination in Eq. (1) used in Ref. 3 affected the results. Indeed if we terminate Eq. (1) at a Q value less than 25 $Å^{-1}$ the subpeak at 2.25 Å becomes very small or even disappears.

B. A possible mechanism of charge transport and magnetic ordering

It is noteworthy that in Figs. 10 and 11 the data of $N_{\text{Mn-O}}$ and $\rho_0 g$ at $r=2.75$ Å at $T=10$ K are continuous through the M-I transition around 17%, and local JT distortions persist even in the metallic phase. A similar behavior was observed recently for the La-Ca system.[45] Small ambiguities in the range of **r** to define the first PDF peak discussed above simply shifts the $N_{\text{Mn-O}}$ versus x plot vertically, and the continuity through the M-I transition is not affected. This is highly counterintuitive, since usually as soon as the metallic state is reached polarons disappear, because the high dielectric constant of the metallic state destabilizes the local bound state. However, the continuity of the 10 K data through the M-I transition indicate that there is no ''sharp'' change in the local structure and the three-site polaronlike distortions do not disappear with the transition. How could polaronlike lattice distortions be compatible with metallic conduction?

The key to solve this conundrum is provided by the information on the dynamics of the local lattice distortion discussed above. Even though the TOF spectrometer does not have energy resolution, because of the Placzek shift important information on dynamics can be obtained from the TOF spectrum. It was found that the dynamics of the local distortion is *slower* than the neutron dynamics of the spectrometer up to 15% of Sr, becomes faster and observable by neutrons at 15% Sr, and *slows down again* in the metallic state at higher Sr concentrations. This means that the energy scale of the local lattice fluctuation is about 10–20 meV only around 15% Sr, and is much slower either side of this composition. Therefore, it is safe to conclude that in the metallic state the lattice dynamics does not follow the carrier dynamics. Charge carriers move swiftly, and the slow dynamics of lattice fluctuation is decoupled from the charge and is not expected to control the charge dynamics. In this sense it is not correct to call these distortions in the metallic state polarons, either small or large, since the charges are no longer trapped by the lattice deformation. It is unclear, however, why the same size of local distortion, three Mn sites per hole, is maintained well into the metallic phase as shown in Fig. 8.

This is in stark contrast to the state below the M-I transition, where the charge and lattice distortions are strongly coupled and they move together as a polaron.

Urushibara *et al.*[15] have shown that in $La_{1-x}Sr_xMnO_3$ the conductivity in the metallic phase depends strongly on composition. Their low-temperature conductivity results can be fitted with a power law, $(x-x_c)^{\alpha}$ with $x_c=0.174$ and $\alpha\sim\frac{1}{2}$ up to $x\sim0.3$. Just beyond the M-I transition at x_c the conductivity is relatively low even at low temperatures, indicating strong scattering of charge carriers in the metallic phase. The source of such strong scattering could be the local distortion discussed above. The nearly full JT distortion observed here in the metallic state with the long Mn-O bond as long as 2.23 Å suggests that the valence of a Mn ion at the JT distorted site may be close to $+3$ as in the undoped $LaMnO_3$. The local JT distortion locally splits the e_g band, and consequently more electrons will be attracted to such a site to fill up the lower band making the Mn ion less positive, approaching Mn^{3+}. Then the local band splitting will reduce the local density of states near the Fermi level, making it more energetically costly for an additional hole to occupy such a site. This mechanism explains how the doped holes could be strongly scattered by the JT distorted sites.

In Fig. 8 it is seen that at about 35% of charge doping the local JT distortions disappear and the system becomes a homogeneous metal. Starting from the homogeneous metallic state, as the Sr concentration is lowered below $x=0.35$, locally some sites are JT distorted leading to an increase in the charge scattering and thus an increase in resistivity as seen in the transport data. Further decrease in the number of doped holes lead to further increase in carrier scattering, and eventually to the confinement of some charge carriers and to their Anderson localization and the transition to the insulating state.

Conversely, seen from the insulating $LaMnO_3$ side, the M-I transition could be explained in terms of the overlap of polarons. At low temperatures and low concentrations of the doped holes the polarons would be separated by a matrix with the AFM ordering of spins. Thus the mobility of such a spin-lattice polaron would be quite low. Even though the holes are extended over the three Mn sites within the polaron, they must be essentially small polarons as far as the mobility is concerned.

As the concentration of Sr is increased, polarons will begin to overlap each other. In the case of a single-site polaron the energy cost for placing two holes on the same site must be quite large, of the order of the t_{2g}-e_g splitting. Thus even when two polarons are placed next to each other their charges would be essentially localized, as seen in the charge ordered state. The charge conductivity then would be controlled by the polaron mobility. On the other hand, in the case of the three-site polarons this energy cost of placing two holes on the same polaron is merely the screened Coulomb repulsion energy between the next-nearest-neighbor site, and would be small. The overlapping three-site polarons could form clusters within which holes would move rather freely, without being dragged by the lattice distortion, thus the charge and lattice dynamics will be decoupled. In other words, within such clusters, charges are not in the polaronic state, and move faster than the lattice as discussed above. Thus in these clusters the lattice is static in the time scale for charge dynamics, and the concept such as percolation which is usually used for static state may be applicable.[12,46] In this scenario with the increased doping the density and size of these clusters would increase, and when the volume fraction of these clusters exceeds the percolation concentration, an extended polaron network will be formed, allowing metallic conduction to commence within the network. The volume fraction of the sites without JT distortion at the M-I transition (50%) suggests a two-dimensional percolation of a square lattice.

In the present work we did not study the spatial correlation among the locally distorted sites. We do not know whether the polarons are randomly distributed, or clustered to form microsegregations as suggested by recent calculations.[47] However, the discussions above need little modification even when the polarons are spatially correlated.

Near room temperature the I-M transition occurs at a higher concentration not far from 1/3,[13,15] which is the percolation concentration for a simple cubic lattice.[48] This is consistent with the small-polaron model at $T>T_c$, T_N. The size of the polaron changes continuously with temperature as shown in Fig. 10. The existence of polarons in the metallic phase is consistent with thermopower experiments also where an enhancement of $\alpha(T)$ by a factor of 2 from the expected value is observed in the FM phase.[49] This indicates that there exists some trapping of the charge carriers at low temperatures which is in disagreement with the homogeneous distribution of charge in the metallic phase.

It is most likely that the Mn spins within the three-site polaron are aligned parallel to each other because the hole is shared among the three sites in a manner similar to the double exchange mechanism as discusses above. Percolation through such spin clusters would induce ferromagnetic long-range order. However, the spatial range of spin correlation can be longer than that of the charge correlation.[42] Hence, the magnetic percolation can occur at a slightly lower concentration than the critical concentration for transport, giving rise to a ferromagnetic spin-canted state as is often observed experimentally.[14,15] This model also suggests that even when the FM long-range order is established through the percolation network, locally AFM correlations can remain.[50] This may explain the strong scattering of the spin waves at high temperatures and near the zone boundary.[51] It is interesting to note that the instability of a homogeneous FM phase in the presence of strong electron-lattice coupling was predicted theoretically.[42]

V. CONCLUSION

The study of the local structure of $La_{1-x}Sr_xMnO_3$ presented in this paper has provided rich information directly related to the structural origin of various properties in this system. Using a local structural technique of the pulsed neutron PDF analysis, we demonstrated how the local structure is different from the average crystallographic structure in this mixed-ion system. This difference offers clues to the understanding of the mechanism of conduction and magnetic ordering. In particular, the presence of local JT distortions that are consistent with the lattice polarons has been shown clearly. The results indicate that the polarons are single-site

small polarons above T_c or T_N, while at low temperatures they become more extended and cover three Mn sites.

As the Sr concentration is increased the polarons begin to overlap, leading to the I-M transition. This process may be described in terms of a percolation phenomenon. Surprisingly the local lattice distortions still prevail even in the metallic phase. The carriers are, however, not trapped by the local distortion in the metallic phase judged from the composition dependence of the local lattice dynamics. We conjecture that they move through the regions without the local JT distortion with relative ease. The Mn sites with the JT distortion may be considered as the charge ''forbidden'' regions and spatially confine charge carriers, strongly scattering them and in some cases localizing them. The fully metallic state without local JT distortion is recovered only with the Sr concentration twice as much as needed to induce the I-M transition. This rather surprising conclusion, however, is consistent with various properties. Detailed studies of this unusual metallic phase may provide further insights into unconventional metallic behaviors of various oxides including those of cuprates.

ACKNOWLEDGMENTS

The authors are grateful to E. L. Brosha for providing the samples, to D. L. Price for helpful discussion on the use of the GLAD spectrometer, to W. Dmowski for providing assistance with data analysis, and to R. Mukundan and B. Dabrowski for their help with the TGA analysis and interpretation of the TGA results. They are indebted to A. R. Bishop and H. Röder for crucial discussions and theoretical ideas. They extend their gratitude to Y. Tokura, A. Fujimori, M. Tachiki, A. J. Millis, J. B. Goodenough, K. A. Müller, L. Gor'kov, E. Dagotto, A. Moreo, M. Salamon, S. Ishihara, S.-W. Cheong, Z.-X. Shen, M. Hundley, S. J. L. Billinge, G. H. Kwei, S. D. Conradson, and T. Tyson for informative discussions. The work at the University of Pennsylvania was supported by the National Science Foundation DMR-9300728 and DMR-9628134.

*Present address: Los Alamos National Laboratory, Los Alamos, New Mexico 87545.

[1] Jin, T. H. Tiefel, M. McCormack, R. A. Fastnacht, R. Ramesh, and L. H. Chen, Science **264**, 413 (1994).

[2] A. J. Millis, P. B. Littlewood, and B. I. Shairman, Phys. Rev. Lett. **74**, 5144 (1995).

[3] S. J. L. Billinge, R. G. DiFrancesco, G. H. Kwei, J. J. Neumeier, and J. D. Thompson, Phys. Rev. Lett. **77**, 715 (1996).

[4] H. Y. Hwang, S.-W. Cheong, P. G. Radaelli, M. Marezio, and B. Batlogg, Phys. Rev. Lett. **75**, 914 (1995).

[5] M. F. Hundley and J. J. Neumeier, Phys. Rev. B **55**, 11 511 (1997).

[6] P. G. Radaelli, D. E. Cox, M. Marezio, S.-W. Cheong, P. E. Schiffer, and A. P. Ramirez, Phys. Rev. Lett. **75**, 4488 (1995).

[7] P. G. Radaelli, M. Marezio, H. Y. Hwang, S.-W. Cheong, and B. Batlogg, Phys. Rev. B **54**, 8992 (1996).

[8] T. A. Tyson, J. Mustre de Leon, S. D. Conradson, A. R. Bishop, J. J. Neumeier, and J. Zang, Phys. Rev. B **53**, 13 985 (1996).

[9] C. H. Booth, F. Bridges, G. J. Snyder, and T. H. Geballe, Phys. Rev. B **54**, R15 606 (1996).

[10] G.-M. Zhao, K. Conder, H. Keller, and K. A. Müller, Nature (London) **381**, 676 (1996).

[11] D. Louca and T. Egami, J. Appl. Phys. **81**, 5484 (1997); Physica B **241**, 842 (1997).

[12] D. Louca, T. Egami, E. L. Brosha, H. Röder, and A. R. Bishop, Phys. Rev. B **56**, R8475 (1997).

[13] G. H. Jonker and J. H. Van Santen, Physica (Amsterdam) **16**, 337 (1950).

[14] E. O. Wollan and W. C. Koehler, Phys. Rev. **100**, 545 (1955).

[15] A. Urushibara, Y. Moritomo, T. Arima, A. Asamitsu, G. Kido, and Y. Tokura, Phys. Rev. B **51**, 14 103 (1995).

[16] C. Zener, Phys. Rev. **81**, 440 (1951).

[17] J. B. Goodenough, Phys. Rev. **100**, 564 (1955).

[18] P. W. Anderson and H. Hasegawa, Phys. Rev. **100**, 675 (1955).

[19] P. G. DeGennes, Phys. Rev. **118**, 141 (1960).

[20] T. Egami and S. J. L. Billinge, Prog. Mater. Sci. **38**, 359 (1994).

[21] B. H. Toby and T. Egami, Acta Crystallogr., Sect. A: Found. Crystallogr. **48**, 336 (1992).

[22] B. E. Warren, *X-ray Diffraction* (Dover, New York, 1990).

[23] H. P. Klug and L. E. Alexander, *X-ray Diffraction Procedures for Polycrystalline and Amorphous Materials* (Wiley, New York, 1968).

[24] B. H. Toby, T. Egami, J. D. Jorgensen, and M. A. Subramanian, Phys. Rev. Lett. **64**, 2414 (1990).

[25] S. J. L. Billinge and T. Egami, Phys. Rev. B **47**, 14 386 (1993).

[26] T. Egami, H. D. Rosenfeld, and Ruizhong Hu, Ferroelectrics **136**, 15 (1992).

[27] *International Table of Crystallography* (Kynoch, Birmingham, 1982).

[28] Y. Wu, W. Dmowski, T. Egami, M. E. Chen, and J. D. Axe, J. Appl. Phys. **61**, 3219 (1987).

[29] S. Teslic and T. Egami, Acta Crystallogr. Sect., B (to be published).

[30] D. J. Mikkelson, A. J. G. Ellison, D. L. Price, and T. G. Worlton, Nucl. Instrum. Methods Phys. Res. A **345**, 112 (1995).

[31] G. Placzek, Phys. Rev. **86**, 377 (1952).

[32] R. J. McQueeney and T. Egami (unpublished).

[33] J. F. Mitchell, D. N. Argyriou, C. D. Potter, D. G. Hinks, J. D. Jorgensen, and S. D. Bader, Phys. Rev. B **54**, 6172 (1996).

[34] D. Louca and T. Egami (unpublished).

[35] H. L. Yakel, Acta Crystallogr. **8**, 394 (1955).

[36] O. I. Lebedev, G. Van Tendeloo, S. Amelinckx, B. Leibold, and H-U. Habermeier, Phys. Rev. B **58**, 8065 (1998).

[37] Q. Huang, A. Santoro, J. W. Lynn, R. W. Erwin, J. A. Borchers, J. L. Peng, and R. L. Q. Greene, Phys. Rev. B **55**, 14 987 (1997).

[38] J. J. Hamilton, E. L. Keatley, H. L. Ju, A. K. Raychaudhuri, V. N. Smolyaninove, and R. L. Greene, Phys. Rev. B **54**, 14 926 (1996).

[39] M. Herview, G. Van Tendeloo, V. Caignaert, A. Maignan, and B. Raveau, Phys. Rev. B **53**, 14 274 (1996).

[40] R. D. Shannon, Acta Crystallogr., Sect. A: Cryst. Phys., Diffr., Theor. Gen. Crystallogr. **32**, 751 (1976).

[41] A. Asamitsu, Y. Moritomo, T. Tomioka, T. Arima, and Y. Tokura, Nature (London) **373**, 407 (1995).

[42] H. Röder, J. Zang, and A. R. Bishop, Phys. Rev. Lett. **76**, 1356 (1996).

[43] T. Egami, *Materials and Crystallographic Aspects of HTc-Superconductivity*, edited by E. Kaldis (Kluwer, Dordrecht, 1993), p. 45.

[44] D. Emin, M. Hillary, and N-L. H. Liu, Phys. Rev. B **33**, 2933 (1986).
[45] S. J. L. Billinge (private communication).
[46] L. P. Gor'kov and V. Z. Kresin, JETP Lett. **67**, 985 (1998).
[47] e.g., S. Yunoki, J. Hu, A. L. Malvezzi, A. Moreo, N. Furukawa, and E. Dagotto, Phys. Rev. Lett. **80**, 845 (1998).
[48] R. Zallen, *The Physics of Amorphous Solids* (Wiley, New York, 1983), 170.
[49] W. Archibald, J.-S. Zhou, and J. B. Goodenough, Phys. Rev. B **53**, 14 445 (1996).
[50] A. W. Moudden, L. Vasiliu-Doloc, and A. Revcolevschi, Czech. J. Phys. **46**, 2163 (1996).
[51] J. W. Lynn, R. W. Erwin, J. A. Borchers, Q. Huang, A. Santoro, J. L. Peng, and Z. Y. Li, Phys. Rev. Lett. **76**, 4046 (1996).